Silicon CVD on powders in fluidized bed: Experimental and multifluid Eulerian modelling study

L. Cadoret [a], N. Reuge [a], S. Pannala [b], M. Syamlal [c], C. Coufort [a], B. Caussat [a,*]

[a] *Laboratoire de Génie Chimique, UMR CNRS 5503, ENSIACET/INPT, 5 rue Paulin Talabot, BP 1301, 31106 Toulouse Cedex 1, France*
[b] *Oak Ridge National Laboratory, Computational Mathematics Group, Bldg. 6012, MS-6367, RM-101, Oak Ridge, TN 37831, USA*
[c] *National Energy Technology Laboratory, 3610 Collins Ferry Road, P.O. Box 880, Morgantown, WV 26507-0880, USA*

Abstract

The Computational Fluid Dynamics code MFIX was used for transient simulations of silicon Fluidized Bed Chemical Vapor Deposition (FBCVD) from silane (SiH_4) on coarse alumina powders. FBCVD experiments were first performed to obtain a reference database for modelling. Experimental thermal profiles existing along the bed were considered in the model. 3D simulations provide better results than 2D ones and predict silane conversion rate with a mean deviation of 9% compared to experimental values. The model can predict the temporal and spatial evolutions of local void fractions, gas and particle velocities, species gas fractions and silicon deposition rate. We aim at mid term to model FBCVD treatments of submicronic powders in a vibrated reactor since we have performed experiments proving the efficacy of the process to treat submicronic particles.

Keywords: Fluidized bed; Silicon; Silane; CFD; Modelling

1. Introduction

The Fluidized bed (FB) technology is employed in a wide range of industrial applications, covering the pharmaceutical, food, chemical and petrochemical industries. Coupled with Chemical Vapour Deposition (CVD), this process enables the modification of the surface properties of particles, for instance to protect them from corrosion or to deposit catalytic materials.

In this framework, the understanding and thus the prediction of gas solid hydrodynamics and of reactive mass transfers is essential to find an optimal coating strategy. Nowadays, Computational Fluid Dynamics (CFD) appears as a promising tool. Using an Eulerian model, the hydrodynamics of gas solid flows can be fairly well reproduced [1–6], but only for fluidizable coarse powders. Moreover, the coupling between hydrodynamics and chemical reactions is rarely considered. Gao et al. [4] used a 3D two-fluid CFD model to predict flow and chemical reactions taking place in a FCC riser. Guenther et al. [5] studied the silane pyrolysis in a FB using MFIX. Similarly Syamlal and O'Brien [6] have studied ozone conversion in a FB.

The present work deals with silicon FBCVD on fully fluidizable dense alumina powders. CFD modelling results concerning silicon deposition from silane SiH_4 on dense alumina Al_2O_3 powders will be presented and discussed. Silicon FBCVD experiments have been performed to constitute a data base for the model, as detailed below.

2. Experimental

As presented in Fig. 1, the FBCVD reactor was made of a vertical cylindrical column of stainless steel with an internal diameter of 0.052 m and a height of 0.8 m. It was externally heated by a three-zone electrical furnace and the wall temperatures were monitored by three thermocouples. Several thermocouples were also placed into a tube of 6 mm in diameter inside the reactor. An Inconel™ porous plate was used for the gas distribution. Silane and nitrogen were supplied to the

* Corresponding author.
E-mail addresses: pannalas@ornl.gov (S. Pannala), Madhava.Syamlal@NETL.DOE.GOV (M. Syamlal), Brigitte.Caussat@ensiacet.fr (B. Caussat).

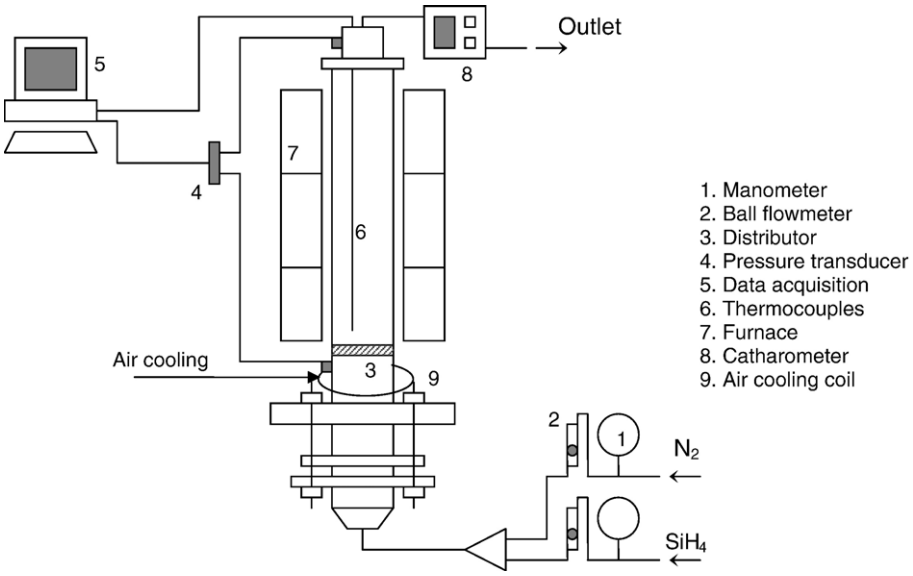

Fig. 1. Experimental setup.

bottom of the bed through ball rotameters connected to manometers. In order to avoid any premature decomposition of silane, the region below the distributor was maintained below 400 °C by air cooling. A differential fast response pressure sensor measured the total pressure drop across the bed. A DasyLab® system enabled the on-line acquisition of the differential pressure and FB temperatures.

The granular material used in this study was non porous alumina particles (Al_2O_3, minimum fluidization velocity U_{mf} = 12 cm/s at 293 K, 7 cm/s at 873 K). Their mean volume diameter was 342 μm (330 μm for the mean Sauter diameter) as measured by laser granulometry (MasterSizer2000).

The operating conditions tested and results obtained are detailed in Table 1. The operating parameters (in particular the bed weight) have been chosen so that the conversion rate was lower than 100% to obtain an experimental database really discriminating for the model. A theoretical thickness was deduced from the deposited silicon mass assuming that the particles were spherical and the deposition was uniform. The conversion rate of silane was deduced from the deposited weight. Elutriation was not considered for the mass balance. Indeed, powders were firstly fluidized by air at high fluidization ratio in order to eliminate the smaller particles and as a consequence elutriation of powder was less than 0.1% of the total bed mass for a typical CVD run duration. Uncertainties of +/− 10% can affect the conversion rates measured.

As detailed in Table 1, the cooling of the region below the distributor is responsible for significant thermal gradients along the bed. They can be decreased till 0.6 °C/cm by increasing the initial bed weight (run A12). Indeed an increase of the FB height improves thermal transfers between the reactor walls and the powders. But the intense circulation of the particles inside the bed guaranteed the uniformity of Si deposition.

The deposition rate varies between 50 and 140 nm/min for the conditions tested. The size distribution of particles has not been affected by deposition. The silane conversion rate and the deposition rate increase with temperature (runs A11 and A5) and with the initial weight of powders (runs A11 and A12). For runs A5 to A12, some moderate and reversible disturbances of the pressure drop and thermal profile along the bed have been observed. They are due to a partial de-fluidisation of the bed, probably related to the appearance of dangling bonds at the surface of powders during deposition generating short lived agglomerates. Such phenomena have been previously observed in literature [7,8]. They did not occur for run A13 because of the low amount of silane injected.

The deposition morphology was analysed by scanning electron microscopy (SEM, LEO 435 VP). In Fig. 2, the presence of

Table 1
Operating conditions and corresponding results

Run	Mean temperature of the bed (°C)	Mean temperature gradient (°C/cm)	Initial weight of powder (g)	U/Umf	Inlet mass fraction of silane	Run duration (min)	Calculated thickness of deposited Si (μm)	Measured silane conversion rate (%)	MFIX silane conversion rate (%)
A5	610	2	800	4.2	0.0615	25	1.95	80.9	76.3
A7	609	2.25	800	4.5	0.1185	21	2.9	65.7	73.1
A11	580	1.5	800	4.1	0.077	40	2.7	59.5	60.6
A12	573	0.6	1300	4.1	0.078	40	2.5	87.7	75.3
A13	610	3	800	4.1	0.0275	60	2.4	97	76.2

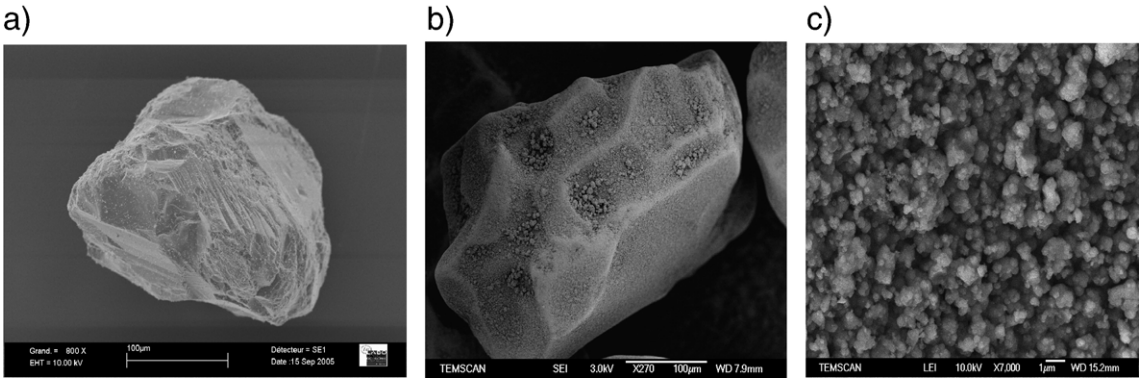

Fig. 2. SEM images of Al_2O_3 particles for run A7 a) before coating. b) after coating. c) after coating, silicon blobs are clearly visible.

small silicon blobs on particles' surface can be observed; they seem to form a continuous layer of hundreds of nanometers thick. Raman and XRD measurements have shown that for the lowest deposit temperatures silicon deposition was mainly amorphous [9]. It tends to become polycrystalline when the temperature increases.

3. Multifluid Eulerian modelling of the process

The CFD open-source code MFIX [10], a benchmark tool for the simulation of FB, was used for this study. The calculations were performed using the continuum model, the drag law of Syamlal-O'Brien [11], the kinetic theory of granular materials with an algebraic form for the granular temperature equation for solid phase stress tensor in the viscous regime, and the Schaeffer model [12] for solid phase stress tensor in the plastic regime. Model equations are listed in Table 2. The model can predict the temporal and spatial evolutions of local void fractions, gas and particle velocities, species gas fractions and silicon deposition rate. Concerning the alumina powders, an internal angle of friction of 40° was considered, corresponding to the repose angle (note that for non-cohesive powders, these two parameters are identical [13]). In the absence of measured values for the coefficient of restitution, a constant value of 0.8 was assumed as for most numerical studies of FB [14].

Some preliminary 2-D and 3-D calculations showed that using the Superbee method for spatial discretization scheme (order 2), the grid independent results were achieved by using 250 cells along the axial direction for a height of 0.5 m, 15 cells along the radial direction for the half diameter, and for 3-D calculations, 6 angular cells. This result is true over all the range of the operating conditions studied.

The operating conditions simulated are those of Table 1, in which are also given the silane conversion rates calculated from 3D simulations. First, thermal profiles existing along the FB and the presence of the tube of 6 mm in diameter along the column axis were included in the simulation. A chemical model was then implemented in the code to simulate the deposition of

Table 2
MFIX equations (see http://mfix.org/documentation/MfixEquations2005-4-1.pdf for the whole set of equations with closure relations)

Governing equations	
Continuity equations for solids phases $m=1$, M	$\frac{\partial}{\partial t}\left(\varepsilon_m\rho_m\right)+\frac{\partial}{\partial x_i}\left(\varepsilon_m\rho_m U_{mi}\right)=\sum_{n=1}^{N_m}R_{\mathrm{mn}}$
Continuity equation for gas phase g	$\frac{\partial}{\partial t}\left(\varepsilon_g\rho_g\right)+\frac{\partial}{\partial x_i}\left(\varepsilon_g\rho_g U_{\mathrm{gi}}\right)=\sum_{n=1}^{N_g}R_{\mathrm{gn}}$
Momentum equations for solids phases $m=1$, M	$\left[\frac{\partial}{\partial t}\left(\varepsilon_m\rho_m U_{mi}\right)+\frac{\partial}{\partial x_j}\left(\varepsilon_m\rho_m U_{mj}U_{mi}\right)\right]=-\varepsilon_m\frac{\partial P_g}{\partial x_i}+\frac{\partial\tau_{\mathrm{mij}}}{\partial x_j}+I_{\mathrm{gmi}}-\sum_{k=1}^{M}I_{\mathrm{kmi}}+\varepsilon_m\rho_m g_i+R_{\mathrm{gm}}\left(\xi_{\mathrm{gm}}U_{\mathrm{mi}}+\overline{\xi}_{\mathrm{gm}}U_{\mathrm{gi}}\right)-\sum_{k=1}^{M}R_{\mathrm{km}}\left(\xi_{\mathrm{km}}U_{\mathrm{ki}}+\overline{\xi}_{\mathrm{km}}U_{\mathrm{mi}}\right)$
Momentum equations for gas phase g	$\left[\frac{\partial}{\partial t}\left(\varepsilon_g\rho_g U_{\mathrm{gi}}\right)+\frac{\partial}{\partial x_j}\left(\varepsilon_g\rho_g U_{\mathrm{gj}}U_{\mathrm{gi}}\right)\right]=-\varepsilon_g\frac{\partial P_g}{\partial x_i}+\frac{\partial\tau_{\mathrm{gij}}}{\partial x_j}-\sum_{m=1}^{M}I_{\mathrm{gmi}}+f_{\mathrm{gi}}+\varepsilon_g\rho_g g_i-\sum_{m=1}^{M}R_{\mathrm{gm}}\left(\xi_{\mathrm{gm}}U_{\mathrm{mi}}+\overline{\xi}_{\mathrm{gm}}U_{\mathrm{gi}}\right)$
Species balance equations for solids phases $m=1$, M	$\frac{\partial}{\partial t}\left(\varepsilon_m\rho_m X_{\mathrm{mn}}\right)+\frac{\partial}{\partial x_i}\left(\varepsilon_m\rho_m U_{\mathrm{mi}}X_{\mathrm{mn}}\right)=\frac{\partial}{\partial x_i}\left(\varepsilon_m\rho_m D_{\mathrm{mn}}\frac{\partial X_{\mathrm{mn}}}{\partial x_i}\right)+R_{\mathrm{mn}}$
Species balance equation for gas phase g:	$\frac{\partial}{\partial t}\left(\varepsilon_g\rho_g X_{\mathrm{gn}}\right)+\frac{\partial}{\partial x_i}\left(\varepsilon_g\rho_g U_{gi}X_{\mathrm{gn}}\right)=\frac{\partial}{\partial x_i}\left(\varepsilon_g\rho_g D_{\mathrm{gn}}\frac{\partial X_{\mathrm{gn}}}{\partial x_i}\right)+R_{\mathrm{gn}}$
Algebraic granular energy equation	$\Theta_m=\left\{\frac{-K_1\varepsilon_m D_{\mathrm{mii}}+\sqrt{K_1^2\left(D_{\mathrm{mii}}\right)^2\varepsilon_m^2+4K_4\varepsilon_m\left(K_2\left(D_{\mathrm{mii}}\right)^2+2K_3\left(D_{\mathrm{mij}}D_{\mathrm{mij}}\right)\right)}}{2\varepsilon_m K_4}\right\}^2$
Syamlal and O'Brien Drag correlation [14]	$\beta_{\mathrm{gm}}=\frac{3\varepsilon_m\varepsilon_g\rho_g}{4V_{\mathrm{rm}}^2 d_{\mathrm{pm}}}\left(0.63+4.8\sqrt{V_{\mathrm{rm}}/Re_m}\right)^2\lvert u_g-u_m\rvert$

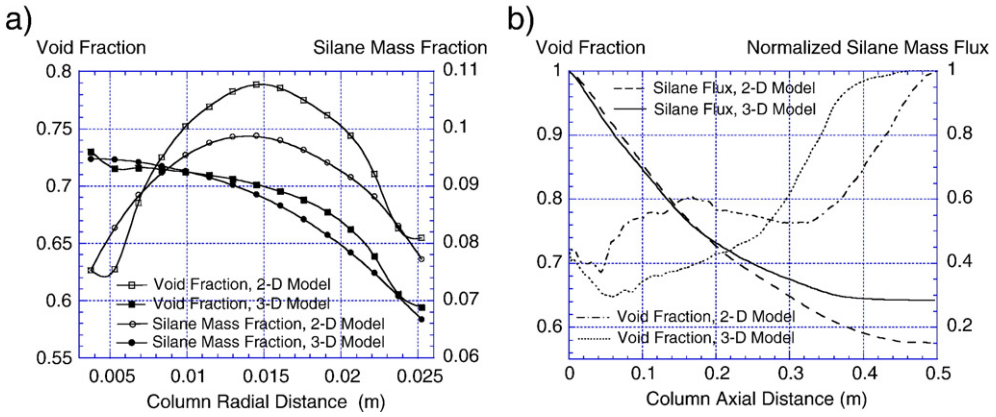

Fig. 3. a) Radial profiles of void fraction and silane mass fraction averaged in time over 2s–7s and on the first 10 cm of the bed for 2-D/3-D calculations — run A7. b) Axial profiles of void fraction averaged on the column section and normalized silane mass flux, both averaged in time over 2s–7s for 2-D/3-D calculations — run A7.

silicon from SiH_4. The kinetic law of Furusawa et al. [15] was chosen because it is applicable for our operating conditions. In the present version of the model, only the overall reaction of silicon deposition from silane is considered, leading to the production of gaseous hydrogen:

$$SiH_4 \rightarrow Si + 2H_2$$

The expression of the reaction rate R_{SiH_4} (kmol m^{-3} s^{-1}) is the following:

$$R_{SiH_4} = (1-\varepsilon_g)\rho_g \frac{k_{s0}(6/d_p)}{1 + K_{H_2}P_{H_2} + K_{SiH_4}P_{SiH_4}} \frac{X_{SiH_4}}{M_{SiH_4}} \qquad (1)$$

where the reaction rate constant k_{s0} (m s^{-1}) and the constants K_{H_2} and K_{SiH_4} (Pa^{-1}) are given by [15] and M_{SiH4} is the molar mass of silane (kg $kmol^{-1}$).

Both 2-D and 3-D simulations were carried out for run A7. As illustrated in Fig. 3, they lead to very different results. Fig. 3(a) shows that the void fraction obtained from the 3-D simulation increases regularly from the column wall to the inner tube wall whereas a maximum of void fraction is predicted at half radius by the 2-D simulation. This is due to the numerical artifact that, with the 2-D model, the voids cannot cross the centerline boundary and are artificially reflected of this symmetric boundary condition. A direct consequence is that the silane mass fraction profiles show similar discrepancies. Guenther et al. [5] had highlighted similar results. Fig. 3(b) indicates that the bed expansion is significantly overestimated by 2-D calculations. Therefore, the gas residence time is longer, silane is more consumed and its outlet mass flux is underestimated by 50% compared to the 3-D simulation. Moreover, a preliminary pure hydrodynamic study showed that MFIX results obtained with 3-D simulations were much closer to experimental mean bed heights and fluctuations [9].

The experimental and calculated conversion rates are in good agreement for runs A5, A7 and A11. Between runs A11 and A5, the effect of the temperature increase on the final conversion rates is correctly reproduced. The conversion rate is also very well predicted for run A11 whereas it is underestimated of 14% for run A12. The calculation predicts indeed a significant increase of the conversion rate of silane due to the greater FB weight, but not sufficiently. For run A13, the initial mass fraction of silane is very low and a high conversion rate of 97% was measured. But once again, the calculation leads to a silane conversion rate of only 76%.

In Fig. 4 the fields of silane mass fraction and of axial gas velocity are presented for this run after 3.6 s of deposition. A slug of gas occupies almost all the upper half part of the bed whereas bubbles are coalescing above the distributor to form

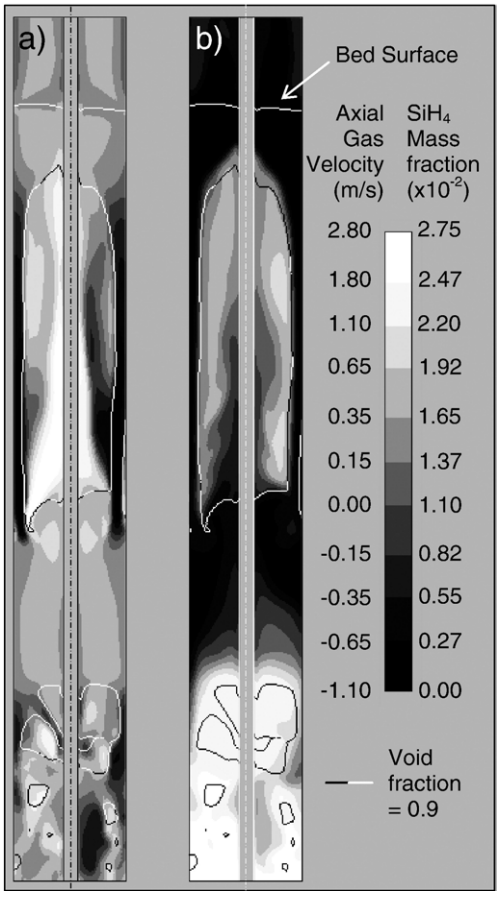

Fig. 4. (a) Axial velocity and (b) silane mass fraction calculated after 3.6 s of deposition — run A13.

another slug. Silane conversion is logically low in these areas but high in denser zones between the slugs. A high flux of gas low in silane penetrates through the bottom of the slug and the richer gas is evacuated towards its periphery. This convective flux and the diffusive flux existing in these zones of high concentration gradient, tend to impoverish the gas present in the slug but not sufficiently to obtain a conversion rate as high as it should be. Further investigations are needed to find the cause of these behaviours. One explanation could be related to the representation of the multicomponent diffusion phenomena into MFIX. Work is now in progress to implement multicomponent diffusion with the MFIX code.

4. Conclusions

Silicon CVD experiments performed in fluidized beds of coarse alumina powders have been simulated in transient conditions using the Computational Fluid Dynamics code MFIX. The model adequately represents silane conversion rates with a global deviation of 9% from experiments. 3D simulations are clearly more physical and appropriate to represent the process than 2D ones. The objectives are now to implement the homogeneous kinetic scheme of silane pyrolysis and the contribution to deposition of unsaturated species such as silylene (SiH_2). Our aim is also to model FBCVD treatments of micronic powders in a vibrated reactor to optimize this technology, since we have performed experiments of vibrated FBCVD of silicon demonstrating the efficacy of the process to treat submicronic particles.

Nomenclature

d_{pm}	Diameter of the particles constituting the *m*th solid phase; m
D_{gn}	Diffusion coefficient of *n*th gas-phase species; m^2/s
D_{mn}	Diffusion coefficient of *n*th solids-phase-m species-n; m^2/s
D_{mij}	Rate of strain tensor, solid-phase; s^{-1}
f_{gi}	Fluid flow resistance due to porous media; N/m^3
g_i	Acceleration due to gravity; m/s^2
i, j	Indices to identify vector and tensor components; summation convention is used only for these indices
I_{gmi}	Gas/solids momentum interface exchange; kg/m^2s^2
I_{kmi}	Solids/solids momentum exchange; kg/m^2s^2
m	Index of the mth solid phase. "m=0" indicates fluid phase
M	Total number of solid phases
n	Index of the *n*th chemical species
N_g	Total number of fluid-phase chemical species
N_m	Total number of solid phases *m* chemical species
P_g	Pressure in the fluid phase; Pa
Re_m	*m*th solids phase particle Reynold number
R_{gn}	Rate of production of the *n*th chemical species in the fluid phase; kg/m^3 s
R_{mn}	Rate of production of the *n*th chemical species in the *m*th solids phase; kg/m^3 s
U_{gi}	Fluid-phase velocity vector; m/s
U_{mi}	mth solids-phase velocity vector; m/s
V_{rm}	Ratio of the terminal velocity of a group of particles to that of an isolated particle; –
X_{gn}	Mass fraction of the *n*th chemical species in the fluid phase
X_{mn}	Mass fraction of the *n*th chemical species in the mth solids phase

Greek letters

β_{gm}	Coefficient for the interphase force between the fluid phase and the mth solids phase; kg/m^3 s
ε_g	Volume fraction of the fluid phase (void fraction)
ε_m	Volume fraction of the *m*th solids phase
Θ_m	Granular temperature of phase *m*; m^2/s^2
ξ_{mk}	$\xi_{mk}=1$ if $R_{mk}<0$; else $\xi_{mk}=0$
ρ_g	Microscopic (material) density of the fluid phase; kg/m^3
ρ_m	Microscopic (material) density of the mth solid phase; kg/m^3
τ_{gij}	Fluid-phase stress tensor; Pa
τ_{mij}	Solid phase *m* stress tensor; Pa

Acknowledgements

Simulations presented in this paper were carried out with the help of I. Touche from LGC, using the Grid'5000 experimental testbed, an initiative from the French Ministry of Research through the ACI GRID incentive action, INRIA, CNRS and RENATER and other contributing partners (see https://www.grid5000.fr). This project has been supported by the French ANR-Réseau National Matériaux et Procédés. SP and MS acknowledge the support of U.S. DOE's Fossil Energy program.

References

[1] J. Ding, D. Gidaspow, AIChE J. 36 (1990) 523.
[2] A.E. Samelsberg, B.H. Hjertager, Int. J. Multiph. Flow 22 (3) (1996) 575.
[3] F. Taghipour, E. Naoko, C. Wong, Chem. Eng. Sci. 60 (24) (2005) 6857.
[4] J. Gao, C. Xu, S. Lin, G. Yang, Y. Guo, AIChE J. 45 (5) (1999) 1095.
[5] C. Guenther, T. O'Brien, M. Syamlal, Fourth International Conference on Multiphase Flows, New Orleans, LA, 2001, p. 1.
[6] M. Syamlal, T. O'Brien, AIChE J. 49 (11) (2003) 2793.
[7] M.P. Tejero-Ezpeleta, S. Buchholz, L. Mleczko, Can. J. Chem. Eng. 82 (2004) 520.
[8] B. Caussat, M. Hemati, J.P. Couderc, Chem. Eng. Sci. 50 (1995) 3615.
[9] L. Cadoret, N. Reuge, S. Pannala, M. Syamlal, C. Rossignol, J. Dexpert-Ghys, C. Coufort, B. Caussat, Colloque Science et Technologie des Poudres, France, Albi, May 2007.
[10] www.mfix.org.
[11] M. Syamlal, T.J. O'Brien, AIChE J. 49 (2003) 2793.
[12] D.G. Schaeffer, J. Differ. Equ. 66 (1987) 19.
[13] K. Terzaghi, Theoretical Soil Mechanics, Wiley, New York, NY, 1942.
[14] M.J.V. Goldschmidt, J.A.M. Kuipers, W.P.M. van Swaaij, Chem. Eng. Sci. 56 (2001) 571.
[15] T. Furusawa, T. Kojima, H. Hiroha, Chem. Eng. Sci. 43 (1988) 2037.